

Stages in spheronisation: evolution of pellet size and shape during
spheronisation of microcrystalline cellulose-based paste extrudates

M.P. Bryan, L.N. Atherton, S. Duffield, S.L. Rough and D.I. Wilson*
Department of Chemical Engineering and Biotechnology, New Museums Site, Pembroke Street,
Cambridge, CB2 3RA, UK

Submitted to

Powder Tech

© MPB, LNA, SD, SLR & DiW

Revised manuscript

October 2014

*Corresponding author

Dr D. Ian Wilson
Department of Chemical Engineering and Biotechnology
New Museums Site
Pembroke Street
Cambridge
CB2 3RA, UK
E-mail diw11@cam.ac.uk
Tel +44 1223 334791
FAX +44 1223 334796

40 Stages in spheronisation: evolution of pellet size and shape during
41 spheronisation of microcrystalline cellulose-based paste extrudates
42

43 M.P. Bryan, L.N. Atherton, S. Duffield, S.L. Rough and D.I. Wilson*

44 Department of Chemical Engineering and Biotechnology, New Museums Site, Pembroke
45 Street, Cambridge, CB2 3RA, UK
46
47
48

49 **Abstract**

50 The stages of extrudate breakup and rounding to form spheroidal pellets was investigated for
51 MCC/water pastes and some MCC/water/calcium carbonate pastes using the interrupted
52 technique reported by Lau *et al.* (2014). A new quantitative parameter, named ‘dumb-bellity’,
53 was developed to monitor the formation and disappearance of ‘dumb-bell’ shaped pellets in
54 the early stages of the rounding process. Tests using mixtures of coloured extrudates
55 confirmed that attachment of small fragments (‘fines’) to the waist of pellets was not
56 responsible for the transition from dumb-bell to more spheroidal shapes. The results
57 confirmed the findings of Lau *et al.*, that rounding was the rate-limiting step. Extrudates
58 prepared with up to 20 wt% calcium carbonate, (the carbonate representing a hard, active
59 pharmaceutical ingredient), were subject to the same spheronisation mechanism. The time to
60 spheronise the carbonate-containing pastes was longer, which could be related to the
61 increased deformation resistance of these materials.
62

63 *Keywords:* breakage, extrusion-spheronisation, microcrystalline cellulose, rounding, shape
64

1. Introduction

Extrusion-spheronisation (E-S) is used in the pharmaceutical sector for manufacturing pellets with high sphericity and density (Haring *et al.*, 2008). E-S is a two-stage process in which the particulate solids are firstly combined with a liquid (the binder) into a paste that is extruded through dies or screens to give cylindrical extrudates, and the extrudates are then spheronised on a rotating friction plate to give pellets (Vervaet *et al.*, 1995; Wilson and Rough, 2007). The term pellet is used here to differentiate the assembly from the constituent particles.

Conine and Hadley (1970) proposed that the basic criterion for successful spheronisation is that the extrudate must be able to break up into sections that are plastic enough to be rounded by the frictional forces on the rotating plate and collisions with pellets and walls. The collisions can also cause attrition, generating fines, which can attach to larger pellets (termed ‘mass transfer’ by Koester *et al.*, 2012). Developing formulations for E-S is complicated, as the paste material must also be malleable enough to be extruded and for pellets to be rounded. It must also be strong enough for extrudates and pellets to retain their shape, and break without creating many fines.

The evolution of pellet size and shape during spheronisation is a complex process and the current level of understanding is mainly at the stage of identifying phenomena, whereas the physics of other granulation methods such as those that employ high shear are well enough understood to allow predictive numerical simulation (*e.g.* Cheong *et al.*, 2007). The three phenomenological models for spheronisation in the literature are summarised in Figure 1.

Model A: Rowe (1985)

Cylindrical extrudates break into short lengths which collide with each other, the friction plate and the walls. The rods undergo plastic deformation which cause them to become rounded cylinders: these are further rounded to a dumb-bell, then to an ellipsoid or egg-shape and finally a sphere.

Model B: Baert et al. (1993)

In addition to breakage, rods are rounded by collisions with the walls and other pellets and become twisted, eventually breaking into sub-pellets with rounded and fractured sides. The latter faces are folded together by the rotating and frictional forces on the

friction plate to form a near-spherical pellet. This folding action was claimed to explain why some pellets contain a cavity.

Model C: Liew et al. (2007)

Pellets pass through the dumb-bell stage and become more round by attachment of fines in the mid-plane or ‘waist’ region of the pellet. Koester *et al.* (2012) also advocated this model, in which attrition generates fines which subsequently re-attach to larger pellets.

All three models emphasise the role played by collisions between pellets and between pellets and the spheroniser surfaces. Fines play a major part in Model C, and this model may be specific to formulations which tend to form fines.

Knowledge of the phenomenology is important as this can guide simulations of pellet breakage and plastic deformation (such as those reported by Sinka (2011)) in constructing quantitative physical models. By comparison, measurement of the distribution of instantaneous pellet positions and velocities is better understood, as a result of development of measurement techniques (*e.g.* Bouffard *et al.*, 2012).

There have been few detailed studies of spheronisation mechanisms to date. This paper employs the approach taken by Lau *et al.* (2014) to investigate the spheronisation of a simple microcrystalline cellulose (MCC)/water paste. E-S formulations of water-tolerant active pharmaceutical ingredients (APIs) regularly incorporate MCC as an excipient, as this ‘gold standard’ material (Koester and Thommes, 2013) provides the paste with good water retention properties and ductility. A similar 45 wt% MCC/water paste was studied: this material has been shown to undergo E-S readily (Zhang *et al.*, 2013).

Lau *et al.* (2014) performed spheronisation tests starting with the same number (20) of identical extrudates, stopping tests after different times in order to measure the number of pellets, their size and shape. With this relatively small number of extrudates, collisions were dominated by wall-pellet events. They found little evidence to support Model B (twisting). Figure 2 summarises the stages that they observed, showing two pathways determined by how the extrudate breaks. When an extrudate broke to give a short rod (length \leq roughly two

extrudate diameters) the rod rounded off, presumably as a result of plastic deformation. Longer rods tended to go through a dumb-bell stage and eventually pass through an approximately elliptical stage en route to a final spheroidal shape. This paper extends the Lau *et al.* study by investigating whether dumb-bell shaped pellets collect fines at their waist (Model C) and to monitor the evolution of dumb-bell shape more explicitly. A simple quantitative measure of dumb-bell shape, termed ‘dumb-bellity’, was created for the latter purpose. This concavity metric is evaluated by analysis of images of individual pellets, which is performed by numerical algorithms in Matlab®. The reliability of this measure, and its sensitivity to imaging and experimental artefacts, is explored. The influence of the initial amount of extrudate loaded into the spheroniser was also investigated.

Application of the results to pharmaceutical formulations is demonstrated by a short investigation of spheronisation of extrudates prepared with calcium carbonate particles in the MCC/water paste. The carbonate is insoluble in water and represents a ‘hard’ active pharmaceutical ingredient (API). Zhang *et al.* (2013) studied the extrusion-spheronisation behaviour of similar formulations, and these new data provide further insight into their results.

2. Materials and methods

2.1 Extrudate preparation

Microcrystalline cellulose (Avicel PH101, FMC Corporation, Ireland) was provided by MSD Devlab (Hoddesdon, UK). The MCC powder characteristics were reported previously by Zhang *et al.* (2011): moisture content ~3 wt%; particle shapes, measured by Malvern Morphologi G3 automated microscope, ranging from small irregular cuboids to larger fibrous rods, with sizes ranging from 2 to 260 µm and Sauter mean diameter of 49.1 µm.

45 wt% MCC/water pastes were prepared following the procedure reported by Zhang *et al.* (2011). Dry MCC powder and deionised water were mixed together using a planetary mixer fitted with a ‘K’-beater attachment and a lid to minimise evaporation (Kenwood Chef KM200, Kenwood Ltd, UK). The mixer had seven speed settings, labelled S1-7, the slowest four of which were used, S1 being the slowest: water was added over 1 min while stirring at S1 and the mass then subjected to a speed/time mixing sequence of S1, 2 min; S2, 3 min; S3, 3 min; S4, 2 min. Material adhering to the bowl was scraped back into the mass with a spatula in between mixing steps. The paste was stored in a sealed plastic sample bag at room

temperature for 4 h before extrusion.

A subset of tests was performed with a grey version of the paste to see whether material transferred between extrudates. Bryan *et al.* (2014) had demonstrated this ‘solid staining’ approach to monitor the formation of static zones in MCC paste extrusion. The paste was prepared by replacing 1% of the MCC powder mass with graphite powder (BDH, size distribution in terms of circle equivalent diameter, d_{CE} , volume basis: $d_{CE,10} = 11.3 \mu\text{m}$; Sauter mean $30.0 \mu\text{m}$; $d_{CE,90} = 51.6 \mu\text{m}$, measured using Malvern Morphologi G3 device). Extrusion tests with the grey paste showed little difference in terms of parameters measured from those obtained for the standard white paste.

Tests with calcium carbonate as a model API were performed with pastes containing (i) 10 wt% and (ii) 20 wt% carbonate (calcite, Pumex UK Ltd, Newcastle-under-Lyme, Staffordshire: particle sizes (by laser diffraction, see Zhang *et al.*, 2013) $0.1\text{--}30 \mu\text{m}$, trimodal distribution with modal values 0.4 , 4.7 and $17.2 \mu\text{m}$, Sauter mean diameter $1.3 \mu\text{m}$). The MCC/water ratio was kept constant, at 45 wt%/55 wt%, as above, so that the carbonate served as hard inclusions within a plastic matrix. The carbonate was combined with the MCC in a dry blending step (1 min at lowest speed setting) before adding the water and mixing as above.

Cylindrical extrudates were generated using a Zwick/Roell Z50 strain frame configured to operate as a ram extruder. A detailed description of the apparatus is given in Zhang *et al.* (2011). A ram fitted with a polyethyletherketone (PEEK) tip forced paste from a cylindrical barrel (i.d. 25 or 11 mm) through a concentric, square entry die. The barrel and dies were constructed from 316 stainless steel. Paste was loaded into the barrel, pre-compacted to 0.9 MPa to consolidate the material, then extruded at a steady ram velocity. All tests were performed at room temperature ($20\text{--}25^\circ\text{C}$) and relative humidity normally between 32-58%. Extrudates were covered with a sheet of ‘cling film’ until used in order to minimise water loss by evaporation.

The majority of results reported employed extrudates of diameter, D , equal to 3.5 mm generated by extrusion through a die land of this diameter. Two other dies were also used, with diameters of 2.0 and 1.0 mm, to study the effect of extrudate diameter. The ram velocity was adjusted for each die in order to give a mean extrusion pressure of around 4 MPa. This

approach was taken to generate extrudates with similar stress history, as matching strain history was considered impractical. The die diameters, D , lengths, L , and ram velocities are summarised in Table 1. In each case this protocol yielded long, smooth, cylindrical rods of diameter equal to that of the die. The smallest rods, with $D = 1$ mm, dried out noticeably more quickly if left exposed to the air. This protocol was similar to that employed by Lau *et al.* (2014), where 3.5 mm diameter extrudates were generated with a 47 wt% MCC/water paste and an extrusion pressure of 8 MPa.

Model API extrudates were prepared with the 3.5 mm die, which differs from the protocol employed by Zhang *et al.* (2013). They used a multi-holed die with 137 die holes of diameter 1 mm and length 2 mm, as they were comparing multi-holed ram extrusion with a wiping blade screen extruder. The extrusion pressure experienced by the pastes in the Zhang *et al.* study was lower than those observed here, by a factor of approximately 2: they reported mean extrusion pressures of 2, 2.4 and 3.9 MPa for the MCC/water alone, 10 wt% CaCO₃ and 20 wt% CaCO₃ pastes, respectively. The corresponding values for the single holed 3.5 mm die used in the current study were approximately twice these, at 4.0, 5.3 and 7.7 MPa, respectively. A higher extrusion pressure is expected to give a more compact and stronger extrudate, so that the work required to round a pellet is expected to be greater.

The water content of the pastes was determined by measuring their mass before and after drying in a vacuum oven at 40°C and 100 mbar for 24 h. Separate tests indicated that this was sufficient time for the dry mass to reach a steady value.

2.2 Spheronisation

Spheronisation was performed using the same Caleva Spheroniser 120 (Caleva Process Solutions Ltd, UK) employed by Lau *et al.* (2014). This featured a 119 mm diameter 316 SS cross-hatched friction plate (pyramidal elements on a square pattern, pitch 1.40 mm, height 0.86 mm and width at top 0.50 mm). Detailed spheronisation studies were performed at rotational speeds, ω , of 1200 rpm, corresponding to a plate rim velocity of 7.5 m s⁻¹.

Each spheronisation test employed a starting charge of N_0 (normally 20) identical cylindrical rods of length l_0 cut fresh from the extruded material. The amount of material spheronised was weighed before and after each test (after sieving) to monitor mass loss due to fines, and

the water content was checked after tests to determine any evaporative losses. Rods of equal length were used in order to track breakage: in industrial and regular laboratory practice, the rod length in the feed is not controlled and interpretation of the breakage phase is therefore complicated by collisions between rods of different lengths from the outset.

The time taken to complete spheronisation, t_{end} , for each condition tested was determined initially by trial and error, running a test until all the pellets were spherical or nearly spherical as judged by eye. This was checked by measuring the shape distribution of the pellets afterwards, as described below. The shape factors obtained indicated that the pellets had attained values close of those of a sphere by the time spheronisation was judged by eye to be complete. Tests were subsequently run for shorter times, halted, and the pellets removed for size and shape analysis. A fresh batch of rods was used for each stopping time, t_s . Tests were interrupted to give similar values of the dimensionless stopping time, $t^* = t_s/t_{\text{end}}$. Some tests were repeated in order to confirm reproducibility of the results.

Model API tests were performed with 20 rods of length/diameter ratio 6:1 and were spheronised at 1200 rpm for 176 s, which was t_{end} for the corresponding MCC/water extrudates. Further effort in determining t_{end} was not considered appropriate for this scoping study, as the influence of paste rheology and extrudate strength should also be investigated in detail and is the subject of ongoing work. The model API pellets did not reach acceptable roundness within 180 s at 1200 rpm. This is expected as Zhang *et al.* (2013) found that the 20 wt% carbonate extrudates, prepared at lower extrusion pressure, took 2 min to spheronise at 1600 rpm in the same spheroniser unit. Equal t_{end} values were used here in order to establish the influence of paste formulation.

2.3 Pellet sampling

At the end of each spheronisation test the batch was weighed and the pellets were gently sieved to remove any fines present, as this simplified the pellet shape analysis. A 2 mm mesh was used for 3.5 mm extrudates and a 0.85 mm mesh for the 1 and 2 mm extrudates. The number of pellets obtained, N , is reported as the ratio $N^* = N/N_0$.

The pellets were placed on a sheet of black photographic foil and photographed individually using a digital camera. The scaling factor for the pellet images was determined using several

images of a ruler with 0.5 mm precision, taken using the same camera settings as those used for pellet sampling. This was then converted using simple pixel counting in MATLAB to yield a factor of 123.4 pixels per mm.

3 Pellet size and shape analysis

The images were analysed using the image analysis tools in Matlab[®] (Mathworks, USA) in order to calculate the following parameters. The MATLAB command 'regionprops' (www.mathworks.co.uk/help/images/ref/regionprops.html) was used to identify the ellipse with the same normalised second central moment of area as the pellet projection. The latter was created from the original colour image using Otsu's thresholding method, using MATLAB's 'graythresh' command ([/www.mathworks.co.uk/help/images/ref/graythresh.html](http://www.mathworks.co.uk/help/images/ref/graythresh.html)). Results are provided for selected data sets to illustrate the relationships between these quantitative parameters.

Aspect ratio, AR

This is defined as the ratio of the length of the minor and major axes, b and l , respectively, of a 2-D projection of the pellet:

$$AR = \frac{b}{l} \quad [1]$$

AR for each pellet was calculated using the lengths of the minor and major axes of the fitted ellipse. For standard shapes the thus calculated AR values can deviate from those expected using geometrical arguments, particularly for ones with concave regions or corners. This is demonstrated in Table 2, for a range of rods, ellipses and overlapping sections with dimension ratios relevant to this study. The AR values calculated as described above are presented alongside those obtained using b given (i) the waist of these symmetrical shapes and (ii) their maximum width. Inspection of the values shows very good agreement for convex shapes and poor agreement for those with very narrow waists, *e.g.* the touching circles.

Aspect ratio is of limited use in describing shape (Bouwman *et al.*, 2004). It provides a convenient measure for monitoring breakage of rods (see rectangles in Table 2) but dumb-bell formation tends to increase AR from the value for a rectangle with the same area. For this work, where dumb-bell formation occurs simultaneously with rod breakage, the major axis length was instead used to monitor breakage via the scaled length, l^* , defined as

$$l^* = \frac{l}{D} \quad [2]$$

where D is the extrudate diameter and l is the major axis length obtained from image analysis. This parameter is a form of the elongation ratio, using D rather than b (for the reasons discussed above). The rods charged to the spheroniser featured $l^* = 6.935$, which differs from their ‘geometric’ elongation ratio (*i.e.* true length/true breadth) of 6.

Other shape factors: C , AF and SF

Granulation studies often quantify the approach to spherical shape using the two-dimensional circularity, C , defined thus:

$$C = \frac{4\pi A}{P^2} \quad [3]$$

where A is the projected area of the pellet and P its perimeter, both determined by image analysis. For a sphere, $C = 1$ and AR also approaches unity. There are two salient points to be taken from the calculated circularity values in Table 2. The first is that C calculated for the pure circle is 0.90025 rather than the ideal value of unity, which arises from the discretisation of the shape that would also be introduced by pixelation in experimental images (Saveliev, 2014). The second is that C is not usefully specific in differentiating between ellipses, rods and dumb-bells for the dimension ratios expected here.

Circularity is a relatively crude method for quantifying the approach to a circular or spherical shape, and alternative two- and three-dimensional measures have been discussed at length (*e.g.* Podczek and Newton, 1995). Lau *et al.* (2014) used the shape and angularity factor (SF and AF) analysis presented by Sukumaran and Ashmawy (2001) to differentiate various sands and used to quantify pellet shape. This analysis is used here. Table 2 reports the SF and AF values calculated for the regular shapes using the MATLABTM code described in Lau *et al.* (2014). These two parameters are compared with circularity in Figure 3, from which it can be seen that (i) circularity does not offer an unambiguous differentiation of dumb-bell shapes (represented by necked circles, NC, and overlapping circles, O2-O6) from shorter rectangles and ellipses; (ii) AF , and to a much greater extent, SF , allow differentiation of dumb-bell shapes from ellipses and rectangles.

Inspection of the SF values in Table 2 showed a strong correlation with the AR values which was also present in the experimental data (see Figure 4). The effort expended in calculating

SF values did not appear to offer significantly greater value in identifying dumb-bells, while AR provided a rough estimate of pellet length (which was monitored separately via l^*).

Images of pellets generated from extrudates containing calcium carbonate were also analysed to give the circular equivalent diameter, d_{CE} , which is the equivalent of a circle with the same projected area of the pellet. These values were generated for comparison of the results with those reported by Zhang *et al.* (2013), who presented their sizing data in terms of d_{CE}/D .

‘Dumb-bellity’ DB

Dumb-bells feature concave regions, which were shown above to be captured with SF . A more direct measure of this shape was developed, inspired by the Hottel’s crossed-strings method employed to calculate view factors in radiative heat transfer. Figure 5(a) illustrates the construction: the smallest convex hull that can be fitted around the 2-D projection is identified and its area, A_{CH} , calculated. This is then compared with the cross-sectional area of the pellet, A , viz.

$$DB \equiv \frac{A_{CH} - A}{A} \quad [4]$$

Shapes which are entirely convex, such as rectangles, ellipses or circles, should give $DB = 0$. During spheronisation DB is expected to start with $DB = 0$, for cylinders, increase with the formation of dumb-bells and then approach zero again as rounding yields spheroidal pellets. Table 2 shows the DB values for the different pellet shapes evaluated (i) analytically, and (ii) numerically. The latter are plotted against SF in Figure 5(b). For the longer ellipses, the calculated DB value deviates from the analytical value of zero, owing to the uncertainty introduced by discretisation discussed above with C for a circle. For the convex shapes (overlapping circles and touching shapes), the numerical values are close to the analytical ones.

The sensitivity of the DB calculation to local irregularities in the perimeter, such as would be introduced by a small fragment (or ‘fine’) sticking to a large pellet, or artefacts introduced by the image analysis perimeter identification, was investigated using a set of images of real pellets. Figure 6(a) shows an example of a pellet, taken from one of the 2 mm trials at $t_s = 3$ s. The DB value, calculated as described above, was 0.14: comparison with Figure 5(b) and Table 2 shows that this is significantly larger than those obtained with regular shapes.

The sensitivity was estimated through the addition of two virtual ‘fine’ pellets to the perimeter of the shape, of a size comparable to the ‘fine’ pellets observed experimentally and approximated as circular in cross section (labelled as ‘F’ at the bottom right of Figure 6(a)). The diameter of the ‘fine’ pellet was 30 pixels. The attachment locations were sampled uniformly from the set of points defining the perimeter, such that approximately 100 points were chosen. The added ‘fines’ were then systematically moved around the perimeter of the shape, taking into account every possible combination of locations. The convex hull was redrawn and *DB* recalculated for each combination.

Figure 6(b) shows the histogram of *DB* values obtained for the pellet in Figure 6(a). The distribution is not regular and shows positive skew at higher *DB* values. The 10%, 50% and 90% percentiles were extracted as parameters of the distribution. Figure 6(c) shows the results obtained for 25 pellets with initial *DB*, protuberance-free, values ranging from 0.01 to 0.15 (Figure 5(b) indicates that $DB = 0.01$ could overlap with elliptical shaped pellets).

A linear trend is evident, with the 50% value lying approximately 0.01 units above the actual *DB* value. The variation, as expressed by the 10th-90th percentiles, is approximately ± 0.015 units. Comparison with Figure 5 shows that some of the overlapping circles (O3-O6) would not be classified as dumb-bells under this criterion: this was considered reasonable as these represent examples of very late stage dumb-bells with little appreciable waist.

The sensitivity of the calculation was also tested for other protuberance sizes. Figure A1 shows the results obtained for the set of images in Figure 6 with ‘fine’ diameters of 15, 60 and 120 pixels. The same linear trend is evident, with the perturbed *DB* values lying further from the original values as the size of the protuberance increases. This result also emphasises the need to remove weakly-attached fines from pellets before conducting automated shape analysis.

Evaluation of *DB* by image analysis was straightforward for pellets generated from $D = 2$ mm and 3.5 mm rods. Rods and pellets generated from $D = 1$ mm extrudates often exhibited larger *DB* values: inspection of the images showed a noticeably large number of bent rods and pellets, which skewed the *DB* calculation. Few of the 2 mm and 3.5 mm rods were bent, which is consistent with the larger cross-section increasing the rods’ stiffness.

4. Results and Discussion

4.1 Mass transfer (Model C)

Collisions between the extrudate rods and the walls generate smaller fragments, termed ‘fines’. Lau *et al.* (2014) reported the mass fraction of initial charge lost to fines and evaporation over the course of a complete spheronisation test reached up to 8%: in this work the fraction was $\leq 5\%$. Re-attachment of fines at the waist of a dumb-bell is an important step in the rounding of larger rods according to Model C (Figure 1). This was investigated here by running a series of tests, for different times, with an equal number of grey and white rods. If re-attachment of fines is not affected by paste colour, there should be a roughly equal number of patches of the second colour at the pellet waist.

Figure 7 presents examples of pellets taken after different spheronisation times for both predominantly white and grey pellets. Both series show the formation of dumb-bells from long rods ($t^* = 0.03-0.10$) and their subsequent rounding via an irregular ellipsoid (reminiscent of a potato, $t^* = 0.10-0.41$) to the final spheroid ($t^* = 1.00$). Neither series shows any preferential increase in the second colour at the waist: if anything, there is more evidence of incorporation of fines at the ends. The final spheroids are dominated by one colour, which was observed in all spheroids generated in these tests. These results indicate that there is some transfer between individual rods by breakage and reattachment, so that a small amount of mixing occurs. The results indicated that Model C, with rounding by fines re-attaching at the waist, does not describe spheronisation with this material under these conditions.

4.2 Effect of rod diameter

Pharmaceutical spheronisation processes tend to employ extrudates with diameters of order 1 mm. Smaller diameter rods are not best suited for the testing protocol employed here as they tend to dry rapidly and bending influences image analysis. Separate tests indicated that 1 mm extrudates had to be sorted, cut and spheronised within 10 minutes before their initial water content reached a significantly different level. Extended spheronisation times also give rise to notable water loss and they also give smaller pellets which are more challenging to image accurately. The effect of rod diameter was studied using 1, 2 and 3.5 mm diameter extrudates: the effect of initial charge size, reported in the next section, employed 3.5 mm pellets.

426

427 Figure 8 summarises the evolution in the number and length of pellets. The 2 mm and 3.5
428 mm data exhibit similar behaviour: rod breakage, accompanied by an increase in N^* and
429 reduction in l^* , is complete by $t^* \sim 0.05$. In this breakage-dominated period the rods break to
430 give about 3 pellets, with l^* around 2 as expected for an initial l^* of 6.935, but with a wide
431 range. Over the subsequent rounding stages l^* approaches 1.35, which is close to the
432 geometric result of 1.44 for a cylinder of initial length to diameter ratio of 6 forming three
433 equal spheres¹. These results are consistent with those reported by Lau *et al.* (2014), who also
434 reported that rod breakage stopped when l^* reached a value of approximately 2.

435

436 The vertical dashed lines in Figure 8 show the approximate boundaries between stages in the
437 spheronisation process. Lau *et al.* (2014) proposed five stages, namely (i) rod break-up, (ii)
438 early dumb-bell, (iii) late dumb-bell, (iv) egg, and (v) spheroidal. In these tests, rod break-up
439 and dumb-bell formation were observed to occur simultaneously so stages (i) and (ii) were
440 combined. The boundaries are similar to those suggested by Lau *et al.*

441

442 The 1 mm diameter rods took longer to reach the plateau values in l^* , up to $t^* \sim 0.20-0.30$ and
443 there is a noticeably larger range in l^* values. Two factors contributing to this behaviour
444 were the drying noted above, which promotes breaking, and the observation that the 1 mm
445 extrudates were small enough to be trapped in the grooves on the spheroniser plate. Video
446 imaging (not provided) showed that rods which lay in the grooves did not undergo any
447 breakage until they were dislodged from the grooves by collision with another pellet. This
448 result is therefore an artefact of the experimental method: in practice, many rods are loaded
449 initially and the relative motion within the toroidal bed on the spheroniser causes regular
450 exchange of pellets from the grooves.

451

452 The change in pellet shape with dimensionless spheronisation time is reported in terms of
453 aspect ratio and dumb-bellity in Figure 9. The AR values for 2 and 3.5 mm rods show a rapid
454 increase during the breakage phase ($t^* \leq 0.05$) and a gradual change thereafter. The use of a
455 logarithmic axis for t^* disguises the fact that rounding takes up the bulk of the spheronisation
456 time. The AR data for the 1 mm rods increase, reflecting breakage, until t^* reaches 0.30, as

¹ Initial volume = $6D \times \pi D^2/4 = 1.5\pi D^3$; volume of three spheres of diameter, $d = 3 \times \pi d^3/6$; $d = \sqrt[3]{3}D = 1.44D$

noted above. The final AR values for all three rod sizes, at 0.95 ± 0.03 , lie within the range of acceptability for coating or tableting applications (Chopra *et al.*, 2002).

As noted above, AR tracks both the general change in shape from rod to spheroid but is not specific for dumb-bell formation. Figure 9(b) shows that the latter can be monitored successfully by the DB parameter. The 2 and 3.5 mm DB values increase from their initial value of zero as soon as breakage starts, reaching values near 0.1 in the rod and early dumb-bell stages, and reducing thereafter to about 0.01 at $t^* \sim 0.15$.

The prevalence of dumb-bell formation in the early stages of spheronisation is demonstrated by Figure 10, where DB is plotted against l^* for each pellet in the sample sets obtained with 2 mm and 3.5 mm extrudates at $t^* \sim 0.05$. The samples were selected from the early dumb-bell stage, after initial break-up was complete, which is indicated by most of the l^* values being less than 2.5. The pellets with small l^* values, near unity, in these plots, correspond to long rods breaking unevenly to give a short and a long rod (see Figure 2). The pellets all exhibit noticeable concavity ($DB > 0.01$). There is a general, increasing trend relating DB to l^* , but no quantitative relationship is suggested as the scatter is significant: fitting linear trend lines to these data sets returned R^2 values of 0.753 ($D = 2$ mm, $N_0 = 20$), 0.489 ($D = 3.5$ mm, $N_0 = 20$) and 0.741 ($D = 3.5$ mm, $N_0 = 40$). At longer times the clusters became more compact and their centroids moved towards the origin ($l^* \sim 1$, $DB \sim 0$) on these plots (data not reported).

The DB values for the 1 mm rods in Figure 9(b) are all noticeably larger, with means reaching 0.16, which is mainly due to bending of rods inflating the value. The trend in DB is consistent with the AR observations. These results suggest that the boundary for the transition from the later dumb-bell to ellipsoid or ‘egg’ stage suggested by Lau *et al.* (2014) could be moved to $t^* \approx 0.20$. Dumb-bells were observed early on in these tests, so the Lau *et al.* scheme has been modified in these plots to merge the ‘rod’ and ‘early dumb-bell’ stages.

4.3 Effect of number of rods

In practice, a spheroniser is charged with many extrudates whose length is not controlled. The effect of N_0 was investigated systematically by spheronising charges of 10, 20 and 40 rods with diameter 3.5 mm and $l/D = 6$ for different t^* and measuring the distribution of size and

shape.

The time taken to spheronise, t_{end} , was found to depend on N_0 . Different initial batch sizes, from $N_0 = 10$ up to and exceeding 160 identical rods, were spheronised to completion (as judged by eye, and confirmed by subsequent *AR* and circularity analysis). Interrupted tests, with detailed analysis of sample size and shape distributions, were not performed in these cases. Figure 11 shows an almost linear increase in t_{end} with increasing N_0 until $N_0 \sim 120$. At higher N_0 (> 180), spheronisation did not proceed to completion as overmassing occurred: the pellets tended to adhere to the spheroniser walls and to each other. At this point the mass of extrudates was approximately 40 g, which is large for a device of this size and is usually avoided as overmassing can occur. Overmassing is postulated to occur as a result of liquid phase being driven to the surface by collision-driven consolidation, favouring the formation of liquid bridge formation between contacting pellets. When the number of pellets is small, water loss by evaporation can reduce the tendency to agglomerate.

The increase in t_{end} with N_0 is attributed to inter-pellet collisions becoming more prevalent as N_0 increases. In collisions with a hard, static wall or moving friction plate, more of the pellet kinetic energy is expected to be dissipated in the form of plastic deformation in the pellet than collisions with another pellet, where the energy is likely to be shared between the pellets. Video observation of the tests with relatively large numbers of rods confirmed that pellets tended to accumulate periodically at the plate circumference. The effect of pellet number on pellet motion requires detailed high speed photography, which was considered to lie outside the scope of this project.

The number of pellets generated was counted in each case, and the N^* value found to be close to $2.75 (\pm 0.10)$ for all N_0 values tested. There was some scatter at $N_0 = 10$ and 20, reflecting small sample sizes, but otherwise very good agreement with larger batches. This is consistent with the results above and suggests that the breakage and rounding processes are not affected significantly, other than in terms of rate, by the number of rods.

The effect of initial rod length was assessed in a simple manner by running tests with a random charge of extrudates. For $N_0 = 80$ and 160, the mass of equal length rods charged to

the spheroniser was recorded and the test repeated afterwards with a batch of unsorted extrudates of the same mass. Figure 11 shows that, for a given value of N_0 , the same final number of pellets was obtained. Similar final pellet size and shape distributions were also obtained (data not reported).

Figure 12 shows that the evolution in particle size (expressed as l^*) and shape (here, AR and DB) followed the trends reported previously. The $N_0 = 10$ data sets do not agree to the same extent as the $N_0 = 20$ and 40 ones, which is attributed to the small number of rods: t_{end} is smallest, and the randomness associated with these stochastic processes (collisions, approach angle, velocity) will then be largest. Figure 12(d) shows a noticeable transition in dumb-bellity as l^* approaches 1.5-1.6, when breakage is less common and rounding takes over. These data confirm the stochastic nature of the breakage and rounding process, which will be a challenge to describe quantitatively in a population balance model.

4.4 Effect of API

The above results provide further confirmation that the mechanism proposed by Lau *et al.* (2014), Figure 2, describes the spheronisation behaviour of these MCC-water pastes. The applicability of the scheme to other paste formulations was studied, briefly, using extrudates containing calcium carbonate, as a ‘hard’ dispersed phase and model API. Addition of the non-deforming phase increases the yield strength and other rheological parameters of the paste, resulting in the increase in extrusion pressure reported in Section 2.1. The plots of l^* , AR and DB against scaled time in Figure 13 shows that the same series of events, of breakage followed by rounding, is followed but the duration of each stage is extended as the level of API increases. The difference in times between the 20 wt% and 10 wt% data sets is noticeably larger than the difference between the carbonate-free and 10 wt% sets, particularly in the DB values. The plot of DB against AR in Figure 13(d), where time is not considered, shows the same transition for all three materials, confirming that the same mechanism is controlling spheronisation.

The difference in timescales for each material in Figure 13 is attributed to the effect of carbonate content on material rheology and collision energies. Lau *et al.* showed that the dependency of t_{end} on spheroniser speed observed in their tests could be explained in terms of the kinetic energy dissipated in collisions. In the tests conducted here the rotation speed and

geometries are similar so the kinetic energy ($\propto \text{mass} \times \text{speed}^2$) increases modestly, via the density of the extrudates and pellets, with increasing carbonate loading. The increase in material yield strength, and thus deformation work that needs to be done in order to change pellet shape, increases more strongly as carbonate is added. Quantifying the change in work is challenging, requiring calculations such as those described by Sinka (2011). As an estimate, let the deformation work be assumed to be proportional to the extrusion pressure, P_{ex} : according to the Lau *et al.* model, t_{end} is proportional to the deformation work and a corrected scaled time, t^+ , is given by

$$t^+ = \frac{t}{t_{\text{end}}(MCC/water)} \frac{P_{\text{ex}}(MCC/water)}{P_{\text{ex}}} \quad [5]$$

It is acknowledged that scaling based on extrusion pressure is unlikely to be an accurate estimate as the die land is not short, so P_{ex} will contain a contribution from die land friction. This factor notwithstanding, Figure 14 shows that these time-scaled data sets show considerable overlap. The 10 wt% API data lie amongst the API-free series, although the number of data points is admittedly small. The 20 wt% API data lie further from the API-free trends, but there is considerable overlap between the range bars and statistically conclusive statements require further work. The larger range of shape parameter values for the 20 wt% API material is also noticeable. Further work is required in order to establish the dependency of the initial, breakage phase on material properties: this approach has assumed that the kinetics of the breakage and rounding phases share the same dependency.

The AR values in Figure 13(b) indicate that the 10 wt% model API pellets are approaching an acceptable degree of sphericity ($AR \geq 0.8$), while nearly 40% of the 20 wt% material lies outside this range. Longer spheronisation times, or higher rotational speeds, are required. Zhang *et al.* (2013) employed a spheronisation speed of 1600 rpm whereas these tests were conducted at 1200 rpm. The difference in speeds, and the use of shorter die lands (lower extrusion pressures), explains how they were able to obtain pellets with AR of 0.88 ± 0.08 within 2 min. Their AR values were calculated by an automated particle sizing algorithm (CantySizer, JM Canty, Dublin) rather than that employed here. They also reported pellet sizes in terms of the ratio of the equivalent circle diameter, d_{CE} , to extrudate diameter, D . Their reported values of $d_{\text{CE}}/D = 1.22 \pm 0.19$ for the 20 wt% API paste were in good agreement with the values obtained for this paste after spheronisation for 880 s.

5. Conclusions

The mechanisms involved in spheronisation of MCC-water based pastes were investigated using the shape and size evolution technique reported by Lau *et al.* (2014). Tests using a mixture of extrudate colours indicated that the pellet rounding mechanism proposed by Liew *et al.* (2007), involving attachment of fines at the waist of dumb-bells, was not a significant feature of spheronisation with this material.

The evolution of size and shape reported by Lau *et al.* (2014) was found to occur with all three extrudate diameters tested. Similar scaled times were observed, with extrudate breakup complete by $t^* \sim 0.05$ and the dumb-bell stage lasting until $t^* \sim 0.15-0.20$. Rounding of ellipsoids takes about 80% of the spheronisation time. The same time scaling was observed with larger numbers of extrudates: the final spheronisation time was found to increase almost linearly with number (or mass) of extrudates until a limit was reached, associated with overmassing (and a different set of phenomena).

The evolution of pellet shape and size was conducted using numerical image analysis. The precision of the calculations was investigated: differences between analytical and numerical values for regular shapes provided confidence indicators for the experimental results. The dumb-bell stage was monitored by a new quantitative shape parameter, named dumb-bellity. This proved acceptably robust for monitoring the appearance and rounding of dumb-bells, and was more discerning than the other shape measures considered.

A short study on the effect of adding ‘hard’ particles to the paste, mimicking an API, confirmed that the spheronisation process followed the same mechanistic steps. The timescales for each step was extended. A simple scaling of time, using extrusion pressure as an indicator of deformation work in the Lau *et al.* model, improved the agreement between data sets for the different materials.

Acknowledgements

Microcrystalline cellulose for this final year student research project was kindly provided by MSD Devlab, Hoddesdon, UK. Jean Bénézech, ENSEIRB-MATMECA, Bordeaux, assisted in the tests with the model API. Support for MPB from Ceratizit GmbH and Sandvik Hyperion is gratefully acknowledged, as are discussions with Vincent Lister.

619 Nomenclature

A	Projected area	m^2
A_{CH}	Area of convex hull	m^2
AF	Angularity factor	-
AR	Aspect ratio	-
b	Minor axis length	m
C	Circularity	-
d_{CE}	Circle equivalent diameter	m
D	Die diameter, extrudate diameter	m
D_b	Barrel diameter	m
DB, DB^*	Dumb-bellity parameter, scaled value	-
l	Major axis length	m
l_0	Initial rod length	m
l^*	Scaled major axis length, $= l/D$	-
L	Die land length	m
m	Mass of pellet	kg
N, N_0	Number of pellets, initial value	-
N^*	Ratio of number of pellets, $= N/N_0$	-
P	Perimeter	m
P_{ex}	Extrusion pressure	Pa
R^2	Correlation coefficient	-
SF	Shape factor	-
t	Time	s
t_s	Time at which test is stopped	s
t_{end}	Time to complete spheronisation	s
t^*	Dimensionless time, $t^* = t_s/t_{\text{end}}$	-
t^+	Pressure corrected scaled time, Equation [5]	-
ω	Spheroniser rotational speed	rpm

620

621 Acronyms

622	API	Active pharmaceutical ingredient
623	E-S	Extrusion-spheronisation
624	MCC	Microcrystalline cellulose
625	PEEK	Polyetheretherketone

References

- Baert, L., Vermeersch, H., Remon, J.P., Smeyers-Verbeke, J. and Massart, D.L., (1993) Study of parameters important in the spheronisation process. *Int. J. Pharm.* **96**, 225–229.
- Bouffard, J., Cabana, A., J. Chaouki, J. and Bertrand, F. (2012) Experimental investigation of the effect of particle cohesion on the flow dynamics in a spheronizer, *AIChEJ*, **59**(5), 1491–1501.
- Bouwman, A.M., Bosma, J.C., Vonk, P., Wesselink, J.A. and Frijlink, H.W. (2004) Which shape factor(s) best describe granules?, *Powder Tech.*, **146**, 66-72.
- Bryan, M.P., Rough, S.L. and Wilson, D.I. (2014) Investigation of static zones and wall slip through sequential ram extrusion of contrasting micro-crystalline cellulose-based pastes, *J. Non-Newtonian Fluid Mechanics*, in press.
- Cheong, Y.S., Mangwandi, C., Fu, J.S., Adams, M.J., Hounslow, M.J. and Salman, A.D. (2007) A mechanistic description of granule deformation and breakage, *Particle Breakage Handbook*, pul. Elsevier.
- Chopra, R., Podczec, F., Netwon, J.M. and Alderborn, G. (2002) The influence of pellet shape and film coating on the filling of pellets into hard sphere capsules, *Eur. J. Pharm. Biopharm.*, **53**, 327-333.
- Conine J.W. and Hadley H.R. (1970) Preparation of small solid pharmaceutical spheres. *Drug Cosm. Ind.*, **106**, 38.
- Haring, A., Vetchy, D., Janovska, L., Krejcova, K. and Rabiskova, M. (2008) Differences in characteristics of pellets prepared by different pelletization methods, *Drug Dev. Ind. Pharm.*, **34**(3), 289-296.
- Koester, M., Willemsen, E., Krueger, C. and Thommes, M. (2012) Systematic evaluations regarding interparticular mass transfer in spheronisation, *Intl. J. Pharm.*, **431**(1-2), 84-89.
- Koester, M. and Thommes, M. (2013) Analysis of particle kinematics in spheronisation via particle image velocimetry, *Eur. J. Pharm. Biopharm*, **83**, 307-314.
- Lau, C. L. S., Yu, Q., Lister, V. Y., Rough, S. L., Wilson, D. I. and Zhang, M. (2014), ‘The evolution of pellet size and shape during spheronisation of an extruded microcrystalline cellulose paste’, *Chemical Engineering Research and Design*, In Press, <http://dx.doi.org/10.1016/j.cherd.2014.01.018>
- Liew, C.V., Chua, S.M. and Heng, P.W.S. (2007) Elucidation of spheroid formation with and without the extrusion step, *AAPS PharmSciTech*, **8**, 1-10.
- Podczec F. and Newton J.M. (1995) The evaluation of a three-dimensional shape factor for the quantitative assessment of the sphericity and surface roughness of pellets, *Intl. J. Pharm.*, **124**, 253-259.
- Rowe, R.C. (1985) Spheronization: a novel pill-making process?, *Pharm. Int.*, **6**, 119-123.
- Saveliev, P. (2014) Lengths of curves, Intelligent Perception website http://inperc.com/wiki/index.php?title=Lengths_of_curves, accessed August 2014.
- Sinka, C.I. (2011) A first order numerical study of the spheronisation process, *Powder Tech.*, **206**, 195-200.

- 667 Sukumaran B. and Ashmawy A. K. (2001) Quantitative characterisation of the geometry of
668 discrete particles. *Géotechnique*, **51**, 1-9.
- 669 Vervaet, C., Baert, L. and Remon, J. P. (1995), 'Extrusion-spheronisation: A literature
670 review', *International Journal of Pharmaceutics*, **116** (2), pp. 131-146.
- 671 Wilson, D.I. and Rough, S.L. (2007) Extrusion-Spheronisation, in *Granulation*, eds. Salman,
672 A.D. and Hounslow, M.J., publ Elsevier, Amsterdam, 189-210.
- 673 Zhang, M., Rough, S. L., Ward, R., Seiler, C. and Wilson, D. I. (2011) A comparison of ram
674 extrusion by single-holed and multi-holed dies for extrusion-spheronisation of
675 microcrystalline-based pastes. *Int. J. Pharm.*, **416**, 210-222.
- 676 Zhang, M., Wilson, D.I., Ward, R., Seiler, C. and Rough, S.L.(2013) A comparison of screen
677 and ram extrusion-spheronisation of simple pharmaceutical pastes based on
678 microcrystalline cellulose, *Intl. J. Pharm.*, **456**, 489-498.
679

1 **Tables: List of table captions**

2 Table 1 Extrusion conditions for different extrudate diameters

3

4 Table 2 Comparison of quantitative measures of pellet shape evaluated. Solid region shows shape:
5 grey line indicates ellipse with equal second central moment of area identified by MATLAB
6 image analysis. The entries were calculated using a square imaging field of side length 1200
7 pixels and the tools employed in the pellet size and shape analysis.

8





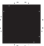








9 Table 1 Extrusion conditions for different extrudate diameters

10

Die land diameter	Die land length	Barrel diameter	Ram velocity
D /mm	L /mm	D_b /mm	mm s ⁻¹
3.5	16	25	1
2.0	16	11	0.5
1.0	16	11	1.2

11

Table 2 Comparison of quantitative measures of pellet shape evaluated. Solid region shows shape: grey line indicates ellipse with equal second central moment of area identified by MATLAB image analysis. The entries were calculated using a square imaging field of side length 1200 pixels and the tools employed in the pellet size and shape analysis.

Label, Shape	Image	Aspect Ratio AR		Circularity C	Shape Factor, SF	Angularity Factor, AF	Dumb-bellity DB	
		Calculated ⁱ	Waist ^j				Analytical	Numerical
E1 Circle		1.00	1.00	1.00	0.00447	0.00009	0	0.00113
E2 Ellipse (2:1)		0.50004	0.5	0.5	0.508	0.0367	0	0.00018
E3 Ellipse (3:1)		0.3332	0.3333	0.3333	0.7152	0.1101		0.0025
E6 Ellipse (6:1)		0.1667	0.1667	0.1667	0.9078	0.3662	0	0.0052
R1 Square		1.00	1.0	1.0	0.5003	0.3103	0	0
R2 Rectangle (2:1)		0.5005	0.5	0.5	0.5661	0.2667	0	0
R3 Rectangle (3:1)		0.3340	0.3333	0.3333	0.6768	0.2999	0	0
R6 Rectangle (6:1)		0.1675	0.1667	0.1667	0.8184	0.3029	0	0
OC1 ^a Touching circles		0.4472	0.00098	0.50	1.0894	1.7487	0.1366	0.1393
OC3 ^a Overlapping circles		0.6686	0.5775	0.6667	0.4170	0.0797	0.0172	0.0190
OC6 ^a Overlapping circles		0.7628	0.7069	0.75	0.2744	0.0346	0.0056	0.0069
NC Necked circles		0.4630	0.3661	0.50	0.6512	0.0600	0.0811	0.0837
Touching squares		0.3786	0	0.5	N.D.	N.D.	0.5000	0.4981

ⁱ AR calculated using length of minor axis of fitted ellipse as b ; ^jwaist (width of major axis bisector) used as b ; ^kmaximum possible width normal to the major axis used as b ; ^aoverlapping circles described by ratio (diameter)/(distance separating centres) so a pair of touching circles is OC1. *Circularity (analytical) for a circle = 1. N.D. indicates not determined.

List of Figure captions

Figure 1 Spheronisation mechanisms according to (a) Rowe (1985); (b) Baert *et al.* (1993); (c) combined deformation and agglomeration mechanism (Liew *et al.*, 2007; Koester *et al.*, 2012).

Figure 2 Phenomenological model for spheronisation of MCC paste extrudates (reproduced from Lau *et al.*, 2014).

Figure 3 Comparison between quantitative measures of pellet shape for geometries in Table 2. (a) angularity factor vs. circularity; (b) shape factor vs. circularity. Labels: NC- necked circles; OC – overlapping circles, number indicates ratio of diameter/separation between centres; E - ellipse, number = AR (E1 is a circle); R - rectangles, number = ratio of length/breadth.

Figure 4 Relationship between SF and AR for (a) regular geometric shapes (see Table 2 for labels) and (b) experimental pellets (mean values at different times). Error bars have been omitted for clarity. Data sets are identified by the number of extrudates, followed by the extrudate diameter. Dashed line in both plots shows the locus $SF + AR = 1$.

Figure 5 (a) Schematic of construction used to calculate dumb-bellity. Dashed line marks extent of convex hull. A is the projected area of the pellet: grey area is the additional area enclosed by the convex hull. (b) Numerical DB values for shapes in Table 2. Dashed horizontal line indicates $DB = 0$. Data labels in Table 2.

Figure 6 Evaluation of sensitivity of DB calculation to perturbations on surface. (a) Image of real pellet (add length scale) showing location of perturbation points on perimeter. Circle labelled F shows size of 30 pixel diameter ‘fine’ attached at two points. (b) Distribution of DB values ($DB^* = DB(\text{perturbed})/DB(\text{no fines})$) calculated for two fines attaching at random points to pellet surface. (c) Effect of adding two particles of 25 pixels to pellets of various starting shapes (examples shown as insets). Error bars show 10% and 90% percentiles.

Figure 7 Selected pellets showing evolution of pellet shape with time. Top row shows pellets with a grey primary pellet, bottom row white. Spheronisation conditions: $D = 3.5$ mm,

$N_0 = 20$ (10 grey, 10 white), $t_{\text{end}} = 180$ s. Scale lines in background are 6 mm apart.

Figure 8 Effect of initial extrudate diameter on dimensionless (a) length and (b) number of pellets during spheronisation. $N_0 = 20$, $t_{\text{end}} = 176$ s. Error bars in (a) indicate the 10th and 90th percentile values. Vertical dashed lines separate the spheronisation stages. At $t^* = 0$, $l^* = 6.953$ and $N^* = 1$.

Figure 9 Effect of rod diameter on evolution of pellet shape, quantified by (a) aspect ratio and (b) dumb-bellity. Error bars show the 10th and 90th percentile values: vertical dashed lines show the spheronisation stages. For $t^* = 0$, $AR = 0.167$ and $DB = 0$.

Figure 10: Correlation between dumb-bellity, DB , and scaled major axis length, l^* , for individual pellets from tests interrupted in early dumb-bell stage.

Figure 11: Effect of spheroniser load on t_{end} for 3.5 mm diameter rods. Symbols: triangles, N_0 counted exactly; circles, N_0 estimated by mass (unsorted extrudates). At high loads ($N_0 > 180$ rods, indicated by vertical dashed line), overmassing occurred and the pellets adhered to each other and the spheroniser walls (see inset photograph).

Figure 12: Effect of spheronisation time and initial spheroniser load on (a) l^* , (b) AR and (c) dumb-bellity. $D = 3.5$ mm. Dashed vertical lines show the spheronisation stages. Error bars show the 10th and 90th percentile values. Plot (d) shows the correlation between DB and l^* .

Figure 13 Effect of calcium carbonate (model API) on evolution of pellet size and shape: (a) scaled length; (b) aspect ratio; (c) dumb-bellity. $D = 3.5$ mm, $N_0 = 20$, 1200 rpm. Scaled time based on $t_{\text{end}} = 176$ s for MCC/water extrudates: t_{end} for API containing pellets was not determined. Plot (d) shows the correlation between DB and l^* .

Figure 14 Evolution of (a) l^* , (b) AR and (c) DB for MCC/water and model API loaded pastes in Figure 13 plotted against rescaled time (Equation [5]).

Figure A1 Sensitivity of dumb-bellity: effect of addition of two artificial fines of diameter (a) 15 pixels, (b) 60 pixels, (c) 120 pixels to 25 particles of various starting shapes. Figure 6(c) shows result for 30 pixels. Error bars show 10% and 90% percentiles.

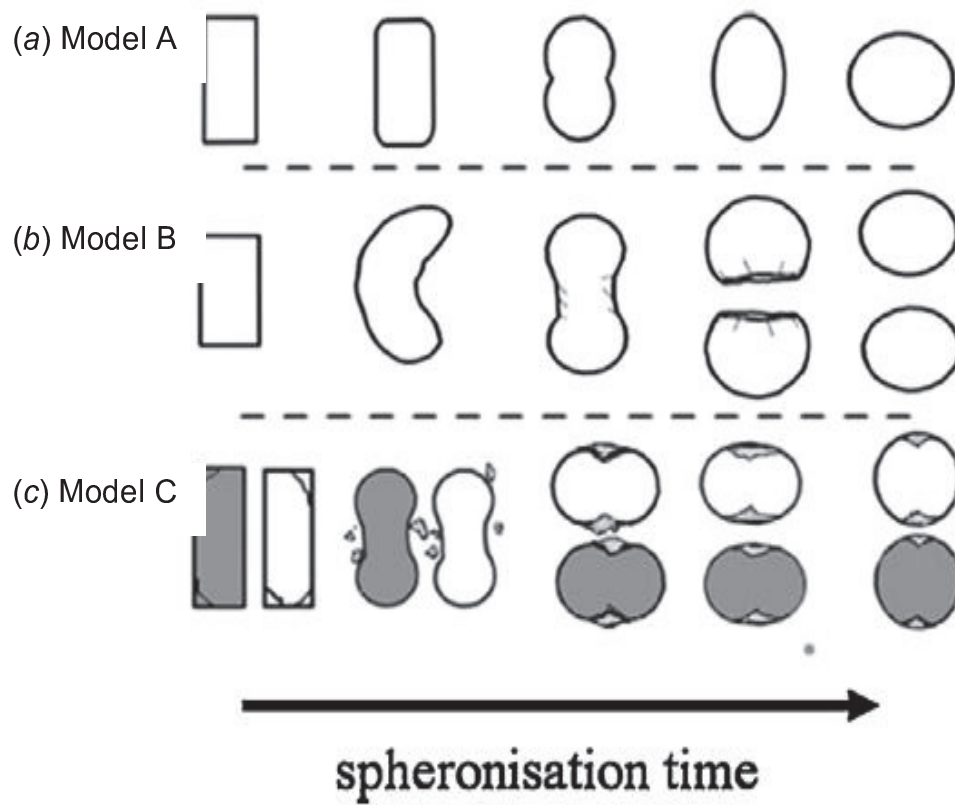


Figure 1 Spheronisation mechanisms according to (a) Rowe (1985); (b) Baert *et al.* (1993); (c) combined deformation and agglomeration mechanism (Liew *et al.*, 2007; Koester *et al.*, 2012).

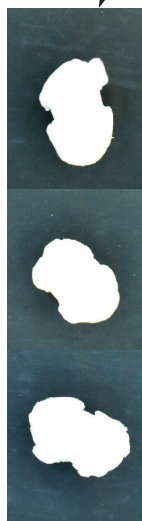
Increasing Spheronisation Time



Extrudate



Extrudate
break-up



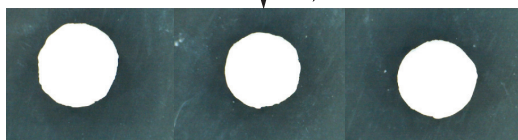
Long rods:
dumb-bells



Short rods:
rounding

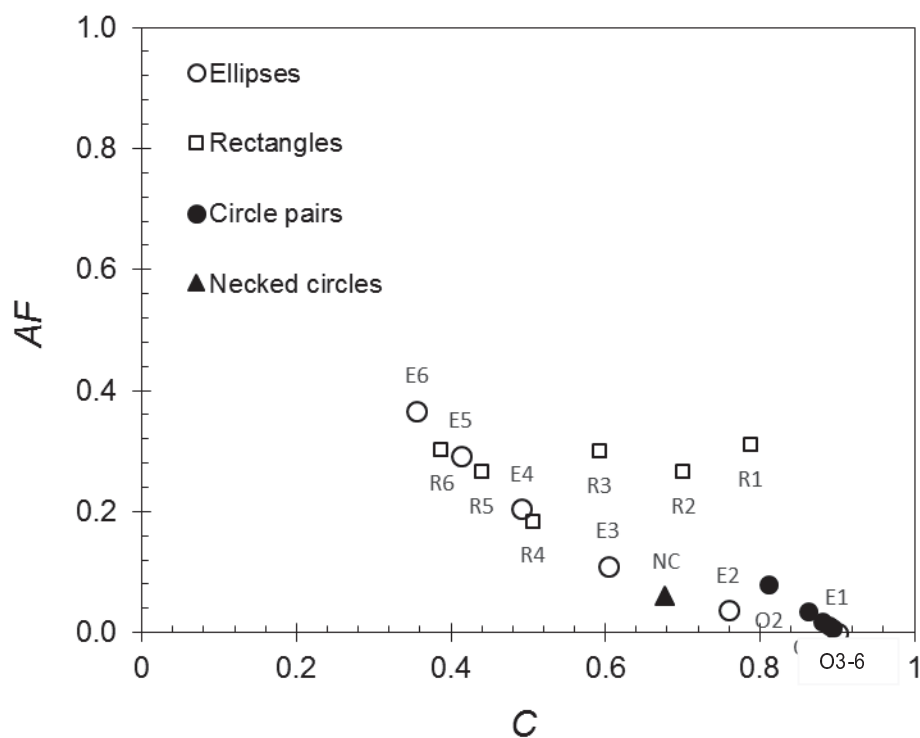


Egg-shaped



Spherical
pellets

(a)



(b)

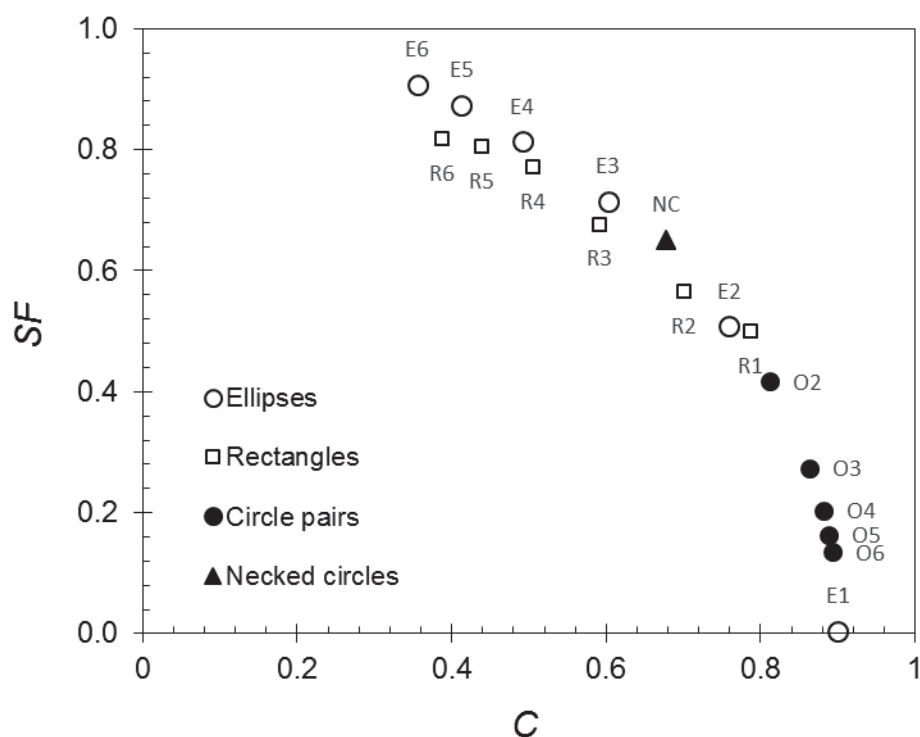
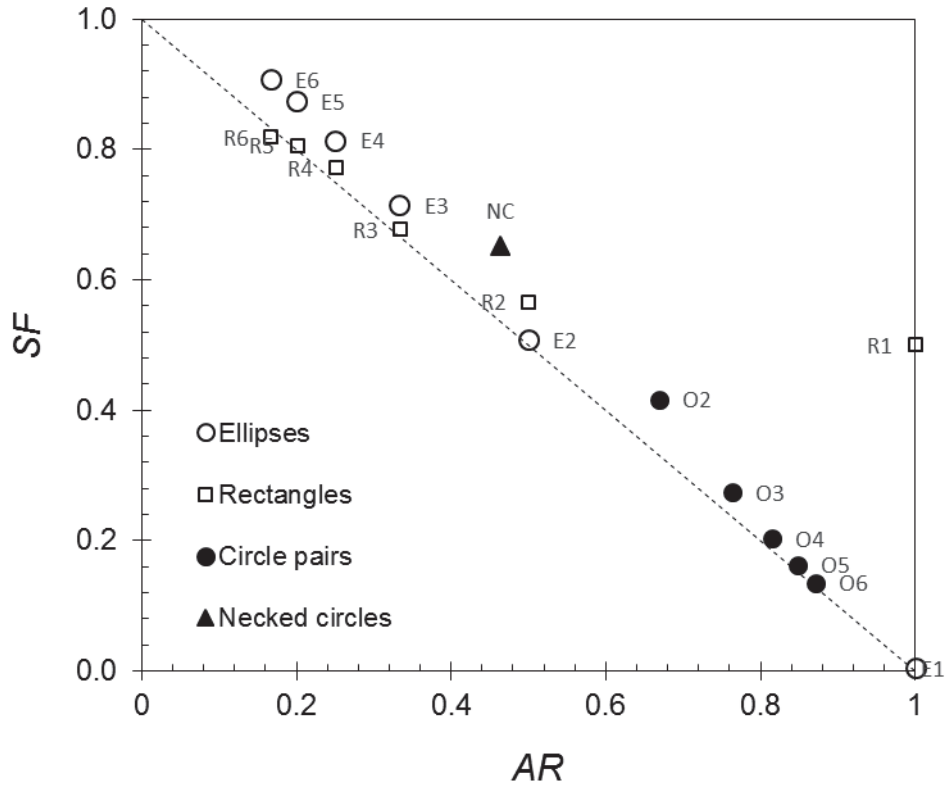


Figure 3 Comparison between quantitative measures of pellet shape for geometries in Table 2. (a) angularity factor vs. circularity; (b) shape factor vs. circularity. Labels: NC- necked circles; OC – overlapping circles, number indicates ratio of diameter/separation between centres; E - ellipse, number = AR (E1 is a circle); R - rectangles, number = ratio of length/breadth.

(a)



(b)

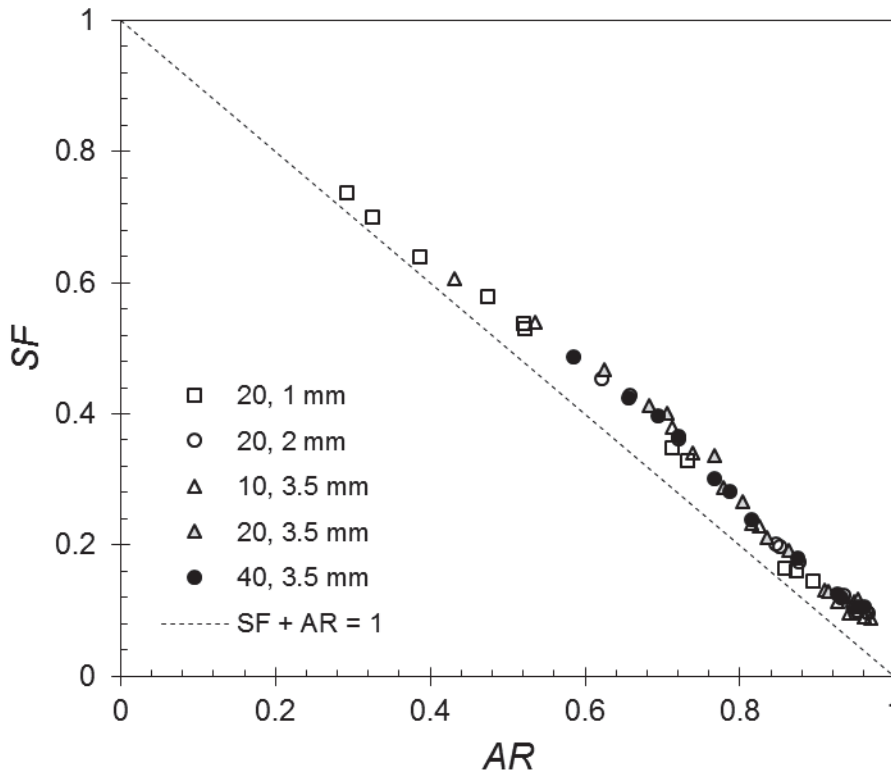
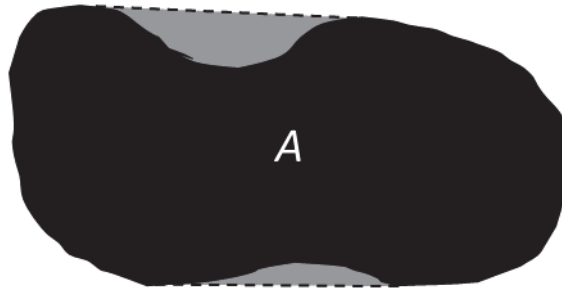


Figure 4 Relationship between SF and AR for (a) regular geometric shapes (see Table 2 for labels) and (b) experimental pellets (mean values at different times). Error bars have been omitted for clarity. Data sets are identified by the number of extrudates, followed by the extrudate diameter. Dashed line in both plots shows the locus $SF + AR = 1$.

(a)



(b)

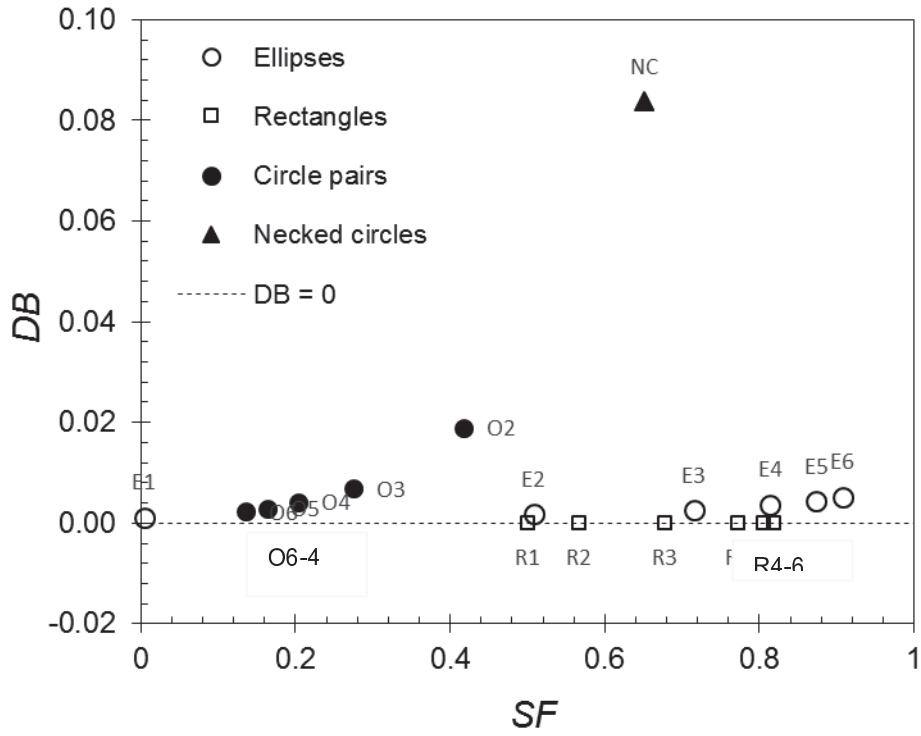
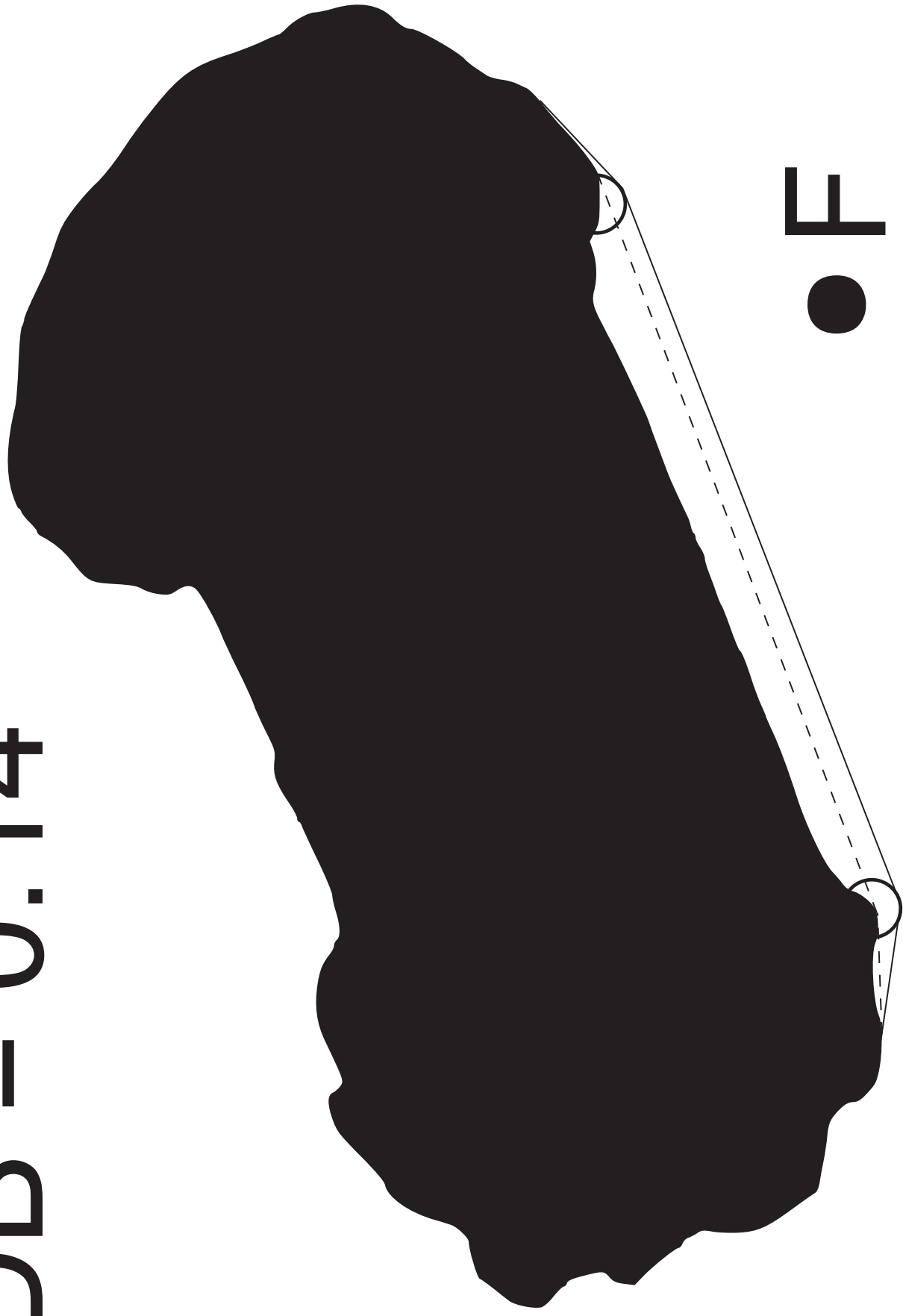


Figure 5 (a) Schematic of construction used to calculate dumb-bellity. Dashed line marks extent of convex hull. A is the projected area of the pellet: grey area is the additional area enclosed by the convex hull. (b) Numerical DB values for shapes in Table 2. Dashed horizontal line indicates $DB = 0$. Data labels in Table 2.

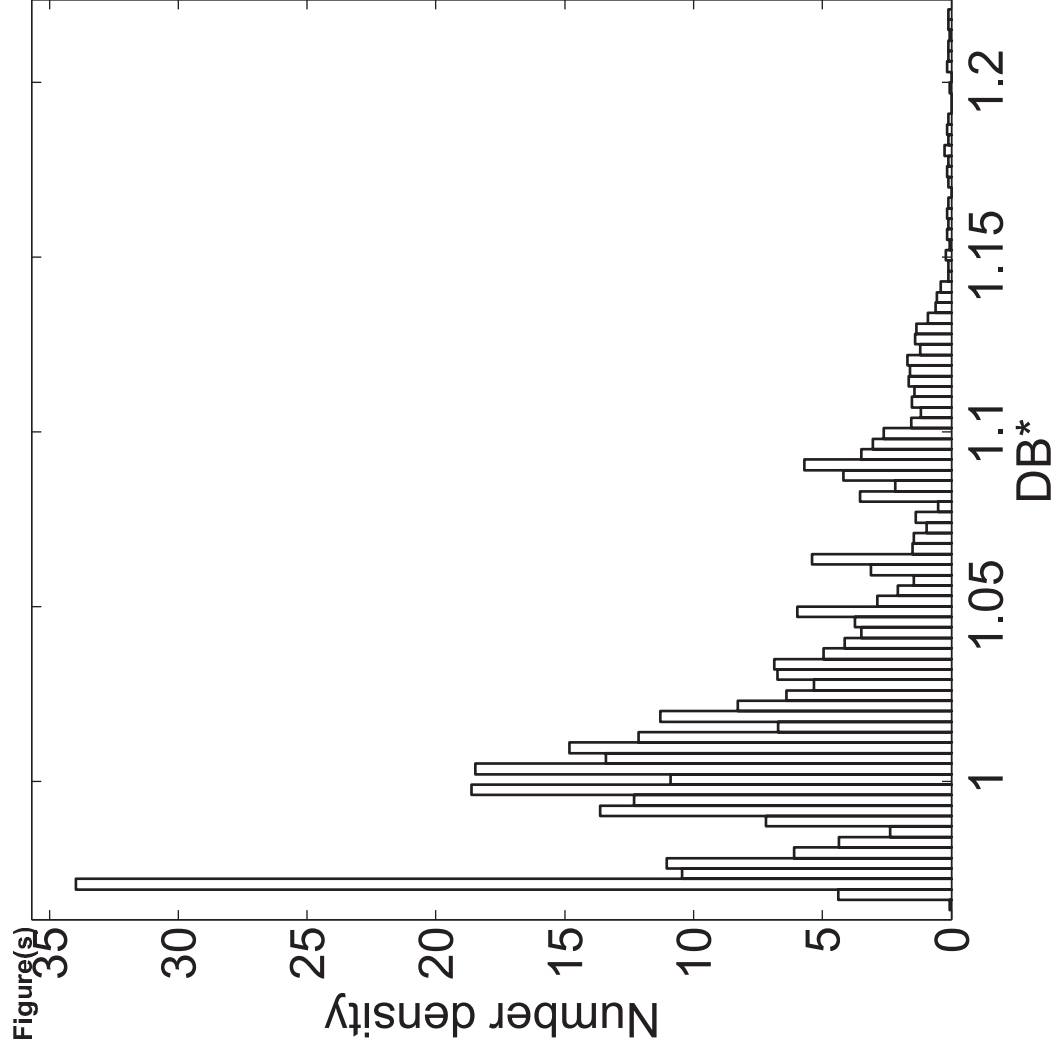
DB = 0.14

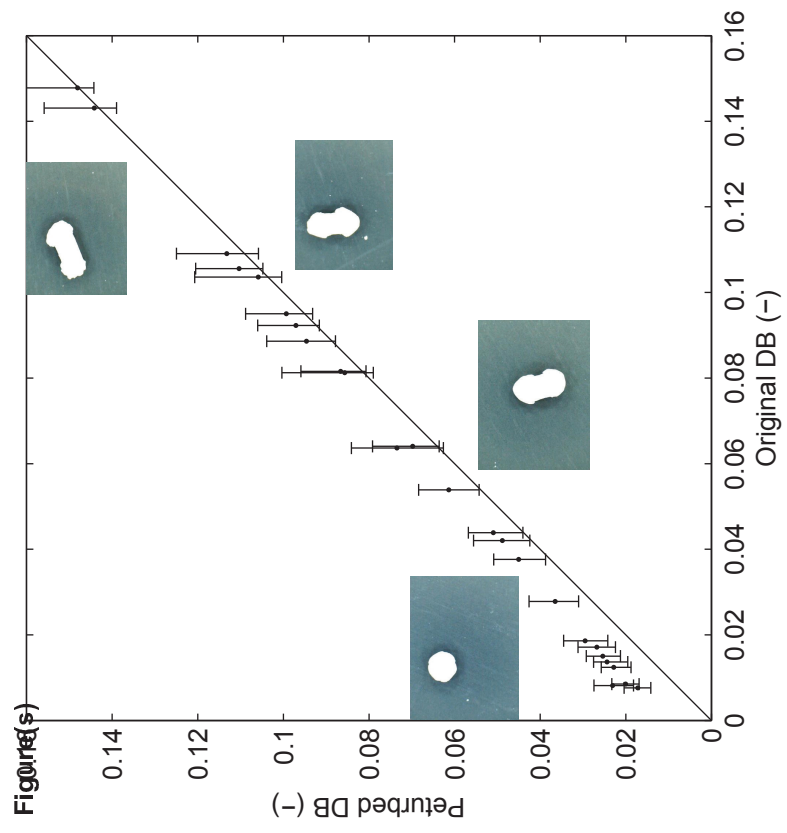
Figure(s)



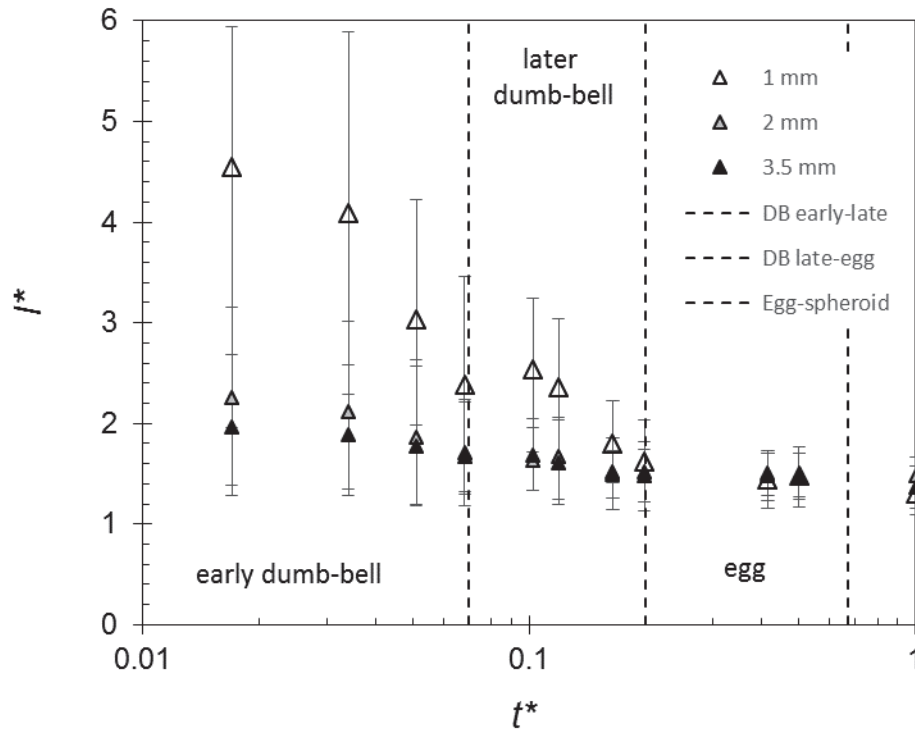
F

2 mm





(a)



(b)

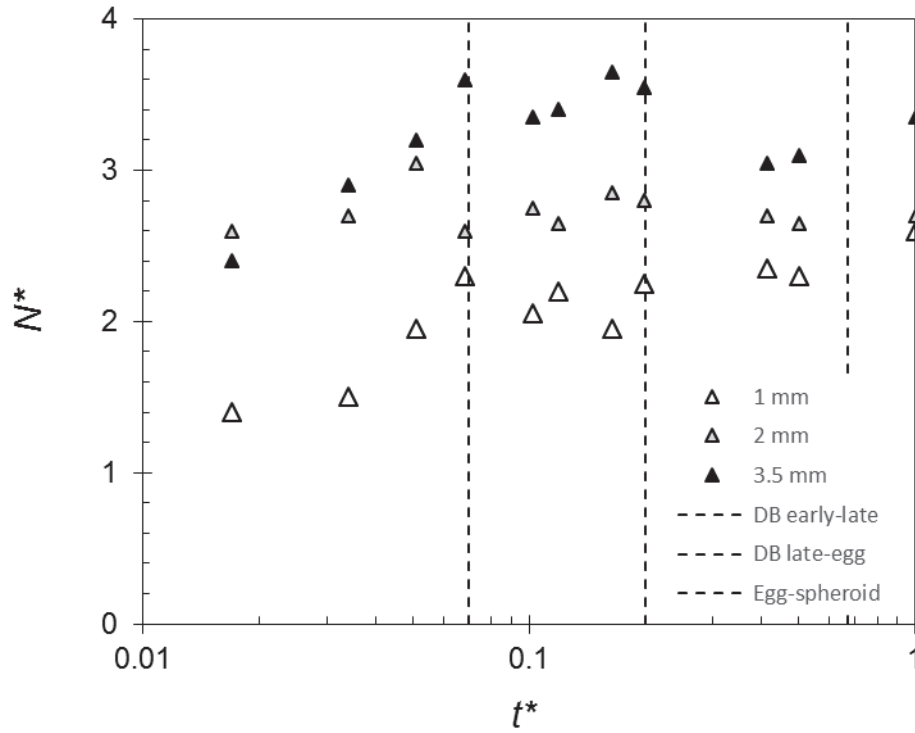
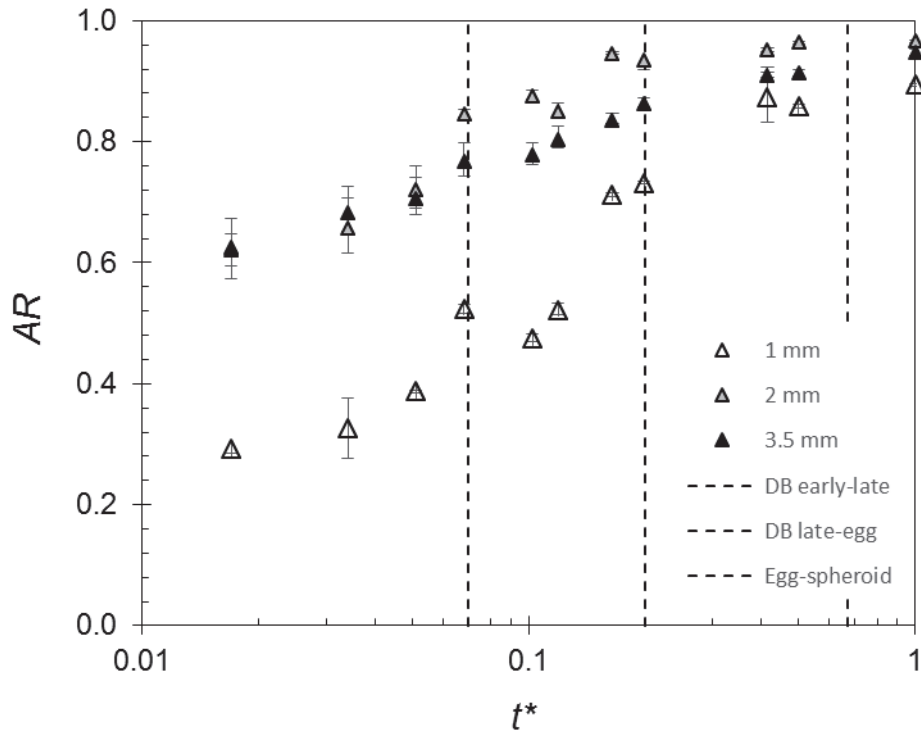


Figure 8 Effect of initial extrudate diameter on dimensionless (a) length and (b) number of pellets during spheronisation. $N_0 = 20$, $t_{\text{end}} = 176$ s. Error bars in (a) indicate the 10th and 90th percentile values. Vertical dashed lines separate the spheronisation stages. At $t^* = 0$, $l^* = 6.953$ and $N^* = 1$.

(a)



(b)

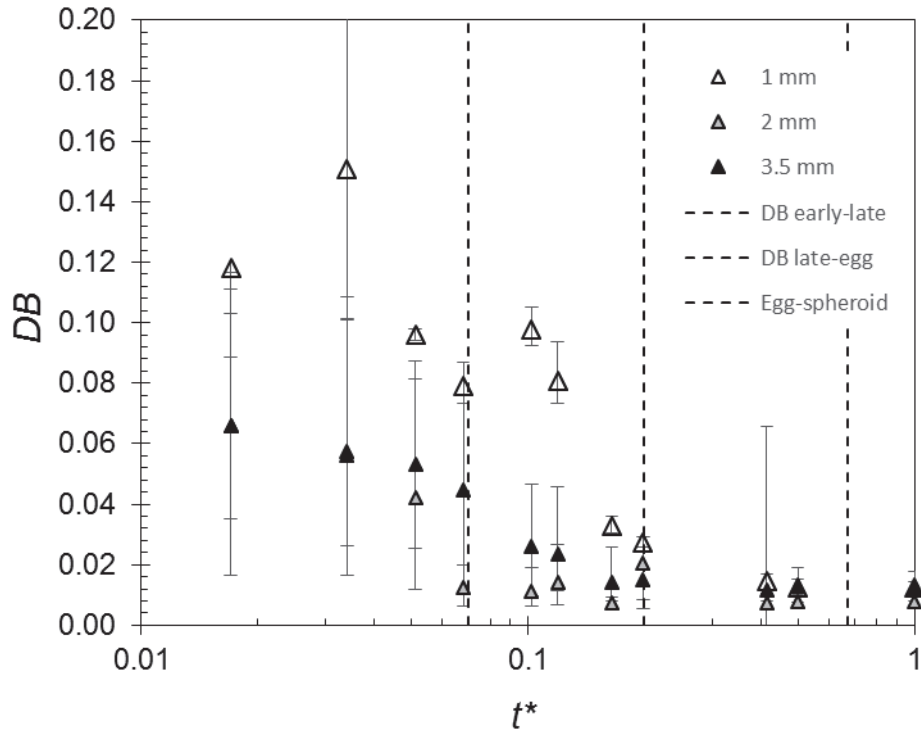


Figure 9 Effect of rod diameter on evolution of pellet shape, quantified by (a) aspect ratio and (b) dumb-bellity. Error bars show the 10th and 90th percentile values: vertical dashed lines show the spheronisation stages. For $t^* = 0$, $AR = 0.167$ and $DB = 0$.

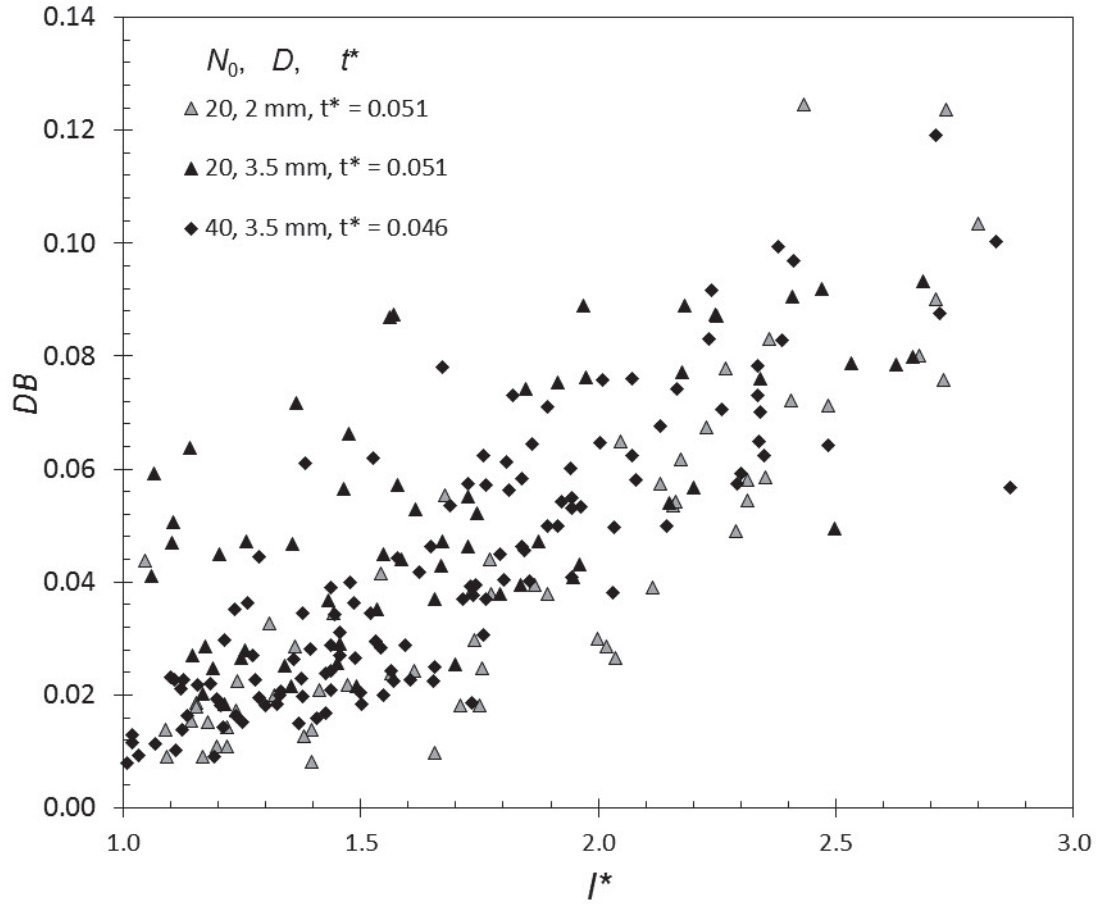


Figure 10: Correlation between dumb-belliness, DB , and scaled major axis length, l^* , for individual pellets from tests interrupted in early dumb-bell stage.

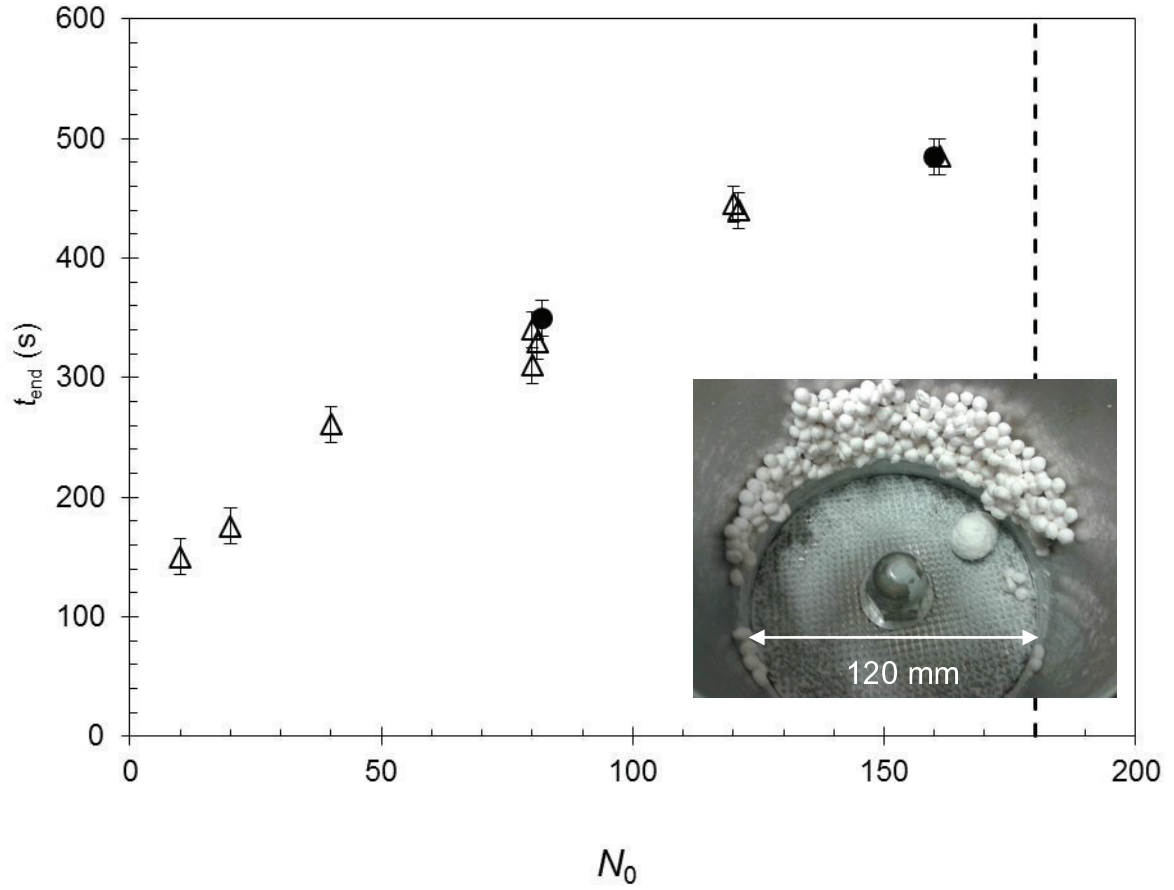
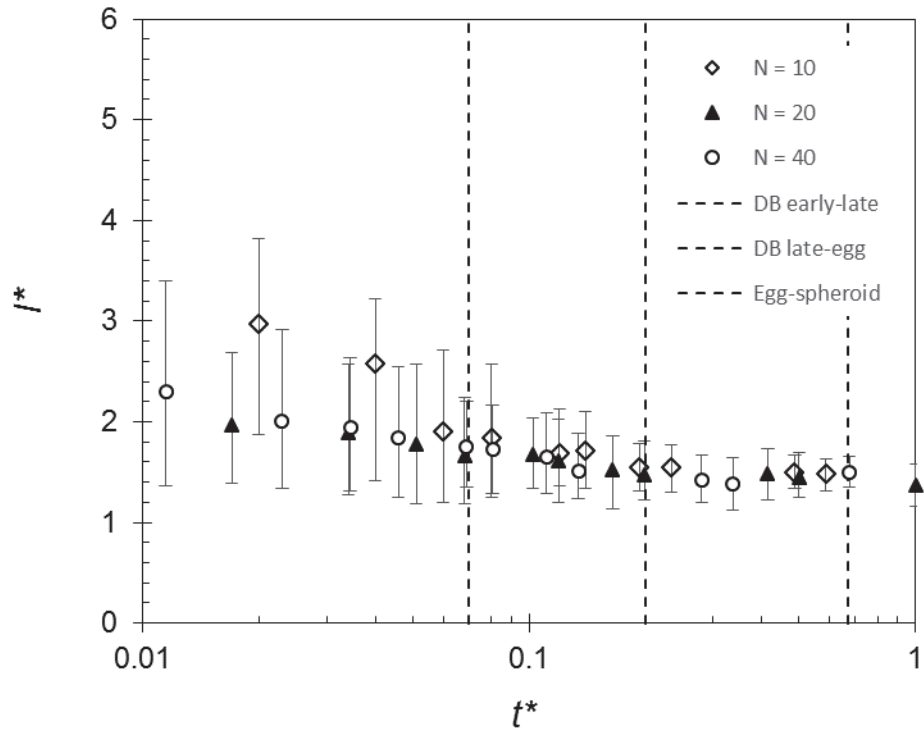


Figure 11: Effect of spheroniser load on t_{end} for 3.5 mm diameter rods. Symbols: triangles, N_0 counted exactly; circles, N_0 estimated by mass (unsorted extrudates). At high loads ($N_0 > 180$ rods, indicated by vertical dashed line), overmassing occurred and the pellets adhered to each other and the spheroniser walls (see inset photograph).

(a)



(b)

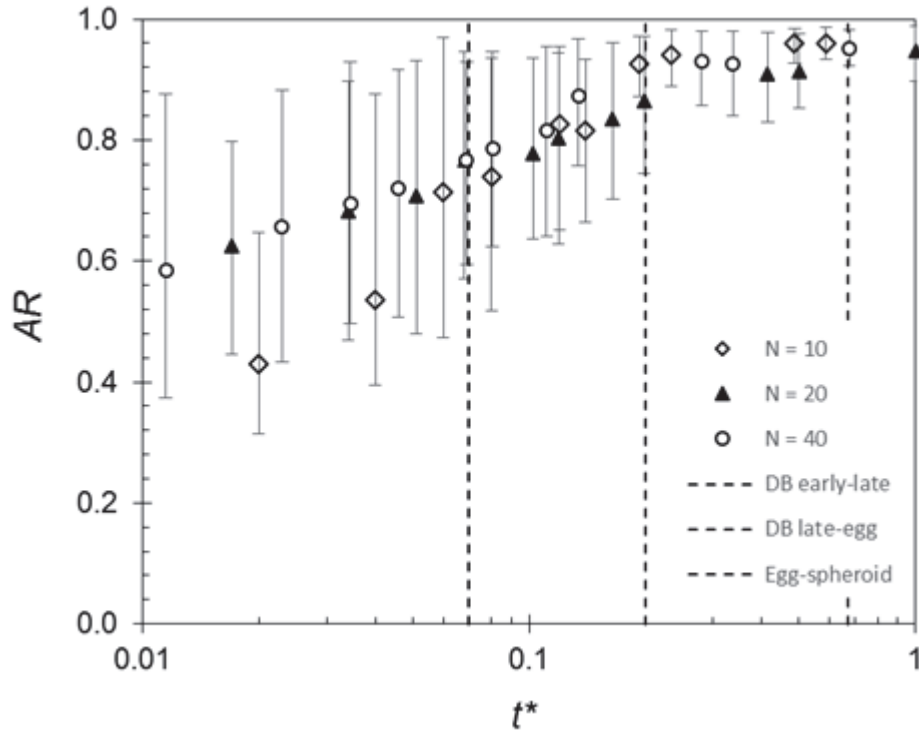
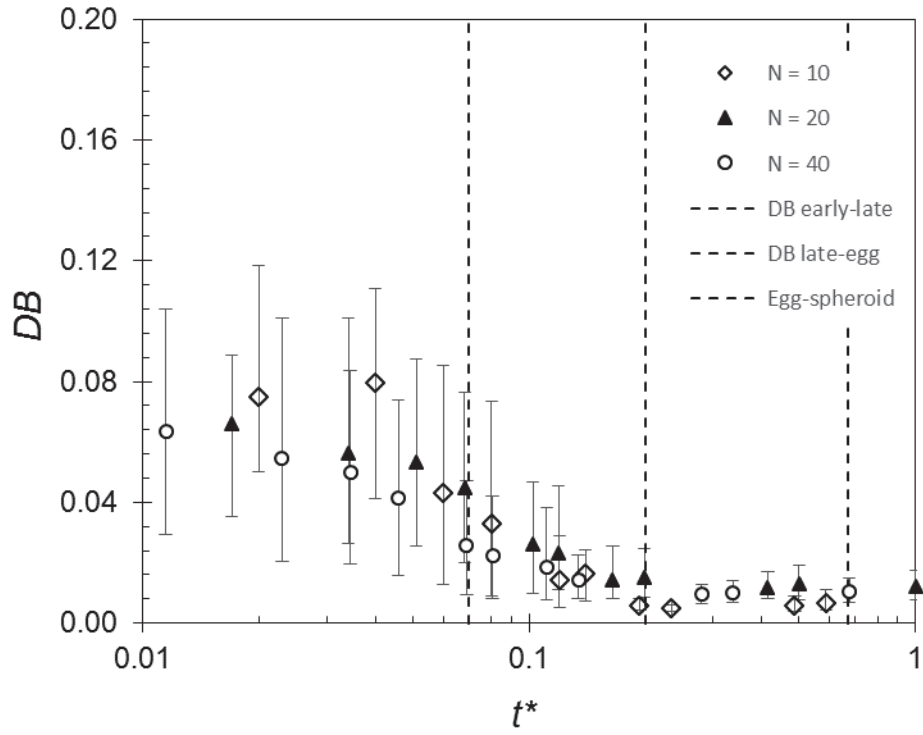


Figure 12: Effect of spheronisation time and initial spheroniser load on (a) l^* , (b) AR and (c) dumb-bellity. $D = 3.5$ mm. Dashed vertical lines show the spheronisation stages. Error bars show the 10th and 90th percentile values. Plot (d) shows the correlation between DB and l^* .

(c)



(d)

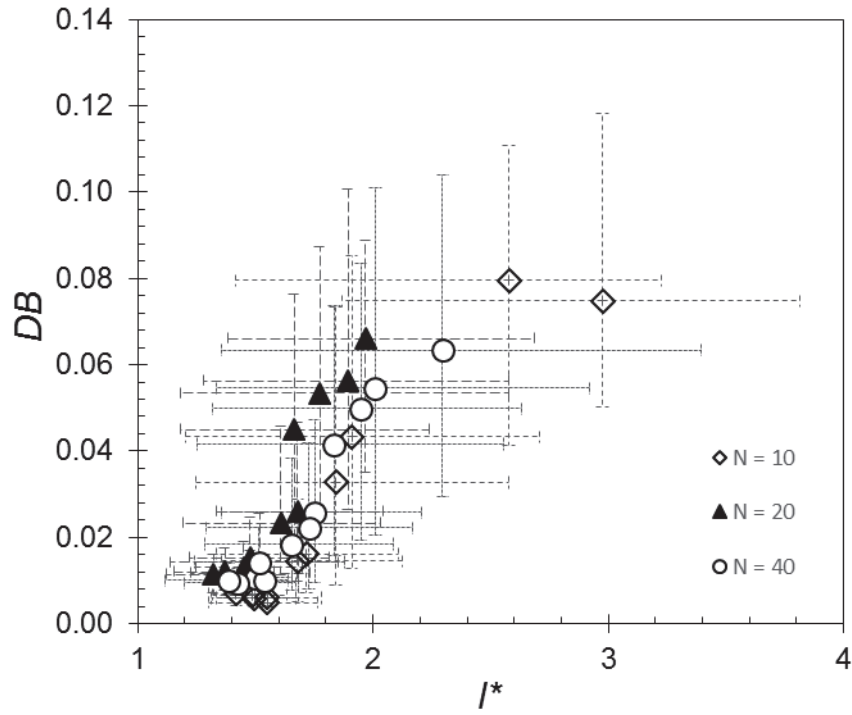


Figure 12: Effect of spheronisation time and initial spheroniser load on (a) l^* , (b) AR and (c) dumb-bellity. $D = 3.5$ mm. Dashed vertical lines show the spheronisation stages. Error bars show the 10th and 90th percentile values. Plot (d) shows the correlation between DB and l^* .

